

# Lyman- $\alpha$ photons through rotating outflows

Maria Camila Remolina-Gutiérrez<sup>1</sup> <sup>\*</sup> & Jaime E. Forero-Romero<sup>1</sup> <sup>†</sup>

<sup>1</sup> *Departamento de Física, Universidad de los Andes, Cra. 1 No. 18A-10 Edificio Ip, CP 111711, Bogotá, Colombia*

26th July 2018

## ABSTRACT

Outflows and rotation are two ubiquitous kinematic features in the gas kinematics of galaxies. Here we introduce a semi-analytic model to quantify how rotating outflows impact the morphology of the Lyman- $\alpha$  emission line. The model is contrasted against Monte Carlo radiative transfer simulations of outflowing gas with additional solid body rotation. We explore a range of neutral Hydrogen optical depth of  $10^5 \leq \tau_H \leq 10^7$ , rotational velocity  $0 \leq v_{\text{rot}}/\text{km s}^{-1} \leq 100$  and outflow velocity  $0 \leq v_{\text{out}}/\text{km s}^{-1} \leq 50$ . We find three important consequences of rotation. First, it introduces a dependency with viewing angle; second it produces a line broadening and third it increases the flux at the line's center. The semi-analytic model reproduces the radiative transfer results for the line width and flux change at the line's center within a 7% and 50% precision for an optical depth of  $\tau_H = 10^5$ , respectively, and within 2% and 1% for an optical depth of  $\tau_H = 10^7$ . The semi-analytic model is a convenient tool to introduce rotational kinematics as a post-processing step of idealized Monte Carlo simulations, providing an easy way to include rotation in models that seek to interpret Ly $\alpha$  spectra in systems where rotation is evident through kinematic maps.

**Key words:** galaxies:ISM — line:profiles — radiative transfer — methods: numerical

## 1 INTRODUCTION

Recent advances in instrumentation have revealed the presence of gas rotation on vastly different physical scales. For instance, spatially resolved spectra on compact dwarf galaxies have measured clear signs of gas showing pure rotation kinematics (Cairós et al. 2015; Cairós & González-Pérez 2017) and the recent mapping of high redshift circumgalactic regions have also revealed kinematic evidence for large scale rotation (Arrigoni Battaia et al. 2018). These systems with star formation, neutral gas and low dust contents naturally produce a Ly $\alpha$  emission line (Partridge & Peebles 1967) motivating the observational work to phenomenologically link H $\alpha$  kinematics to Ly $\alpha$  spectra (e.g. Herenz et al. 2016).

What is then the expected imprint of rotation on a resonant emission line such as the Ly $\alpha$  line? To what extent is it possible to constrain rotational kinematics from the Ly $\alpha$  emission line? Detailed radiative transfer (RT) Ly $\alpha$  modeling of rotating systems started until recently by Garavito-Camargo et al. (2014). In that work the authors studied the influence of pure solid body rotation on the Ly $\alpha$  line's morphology. They found that rotation indeed introduces changes, the most noticeable being the dependence of the

spectra with the viewing angle with respect to the rotation axis.

Garavito-Camargo et al. (2014) also presented a simple semi-analytical approximation that accounted for the main features of the Ly $\alpha$  spectra from a rotation sphere. Recently, this semi-analytic solution was used to perform a Markov Chain Monte Carlo exploration to fit the observed spectra Compact Dwarf Galaxy (Forero-Romero et al. 2018) with atypical features that could be explained by pure rotation.

However, the gas dynamics in Lyman Alpha Emitter (LAE) galaxies are more complex than pure rotation. The case for outflows as traced in the Ly $\alpha$  line is solidly established. In many observations the Ly $\alpha$  line profile has a single peak redwards from the line's center, in other cases there is a double peak but the peak on the red side is stronger (e.g. Steidel et al. 2010; Erb et al. 2014; Trainor et al. 2016). These features have been explained as the consequence of multiple Ly $\alpha$  photon scatterings through a homogeneous outflowing shell of neutral Hydrogen (Verhamme et al. 2006a; Orsi et al. 2012; Gronke et al. 2015).

Nevertheless, a study of the combined effects of outflows and rotation has not been presented in the literature. Here we report on such a study. We investigate a simplified geometrical configuration corresponding to a spherical gas cloud with symmetrical radial outflows and solid body rotation. We base our modeling on a Monte-Carlo radiative transfer code. Besides modeling the impact of joint rotation and

<sup>\*</sup> mc.remolina197@uniandes.edu.co

<sup>†</sup> je.forero@uniandes.edu.co

outflows, we also check to what extent the semi-analytical model presented by [Garavito-Camargo et al. \(2014\)](#) can also be applied in our case.

The structure of the paper is the following. We introduce first our theoretical tools and assumptions in Section 2. We continue in Section 3 with the results from the Monte-Carlo simulation, the comparison against the semi-analytical approximation which we use to make a thorough exploration of the effect of rotation. In Section 4 we discuss our results and their possible implications for observational analysis to finally present our conclusions in Section 5.

## 2 THEORETICAL MODELS

The Monte Carlo code we use (CLARA) ([Forero-Romero et al. 2011](#)) follows the propagation of individual photons through a neutral Hydrogen medium characterized by its temperature, velocity field and global optical depth. The code assumes a homogeneous density throughout the simulated volume. In the current implementation we neglect the influence of dust. Our basic model is an spherical distribution of neutral hydrogen, an approximation commonly used in the literature, as it explains a wide variety of observational features ([Ahn et al. 2003](#); [Verhamme et al. 2006b](#); [Dijkstra et al. 2006](#)).

The velocity field we use captures both outflows and rotation. Outflows are described by a Hubble-like radial velocity profile with the velocity magnitude increasing linearly with the radial coordinate; the outflows model is fully characterized by  $v_{\text{out}}$ , the radial velocity at the sphere's surface. Rotation follows a solid body rotation profile, which is fully characterized by  $v_{\text{rot}}$ , the linear velocity at the sphere's surface.

The total velocity field corresponds to the superposition of rotation and outflows. The cartesian components take the following form:

$$v_x = \frac{x}{R}v_{\text{out}} - \frac{y}{R}v_{\text{rot}}, \quad (1)$$

$$v_y = \frac{y}{R}v_{\text{out}} + \frac{x}{R}v_{\text{rot}}, \quad (2)$$

$$v_z = \frac{z}{R}v_{\text{out}}, \quad (3)$$

where  $x$ ,  $y$  and  $z$  are the cartesian position coordinates with the origin at the sphere's center,  $R$  is the radius of the sphere and the direction of the angular velocity vector is the  $z$  axis.

For each model setup we follow  $10^5$  individual photons generated at the center of the sphere at the Ly $\alpha$  line's center as they propagate through the volume and finally escape. We store the final frequency and propagation direction for each photon at its last scattering.

As input parameters we use  $\tau_{\text{H}} = \{10^5, 10^6, 10^7\}$ ,  $v_{\text{out}} = \{5, 25, 50\}$  km s $^{-1}$  and  $v_{\text{rot}} = \{0, 50, 100\}$  km s $^{-1}$ , for a total of 27 models with all the possible parameter combinations. The range of values have some overlap with the expectations from a galaxy with a total neutral hydrogen mass of  $10^8$ – $10^9$   $M_{\odot}$ . We also define the viewing angle,  $\theta$ , as the angle between the rotation axis and the line of sight of a potential observer.

[Garavito-Camargo et al. \(2014\)](#) presented an analytical model that accounts for the effects of pure rotation on the Ly $\alpha$  line morphology. The basic assumption of their analytical model is that each differential surface element on the sphere Doppler shifts the photons that it emits. In this paper we introduce this ansatz by post-processing the results of the outflows simulations without rotation. The frequency of each photon is Doppler shifted as follows

$$x' = x + \frac{\vec{v}_{\text{rot}} \cdot \hat{k}}{v_{\text{th}}} \quad (4)$$

where  $x'$  is the photon's new adimensional frequency,  $x$  is the photon's frequency after being processed only by the outflow,  $v_{\text{rot}}$  is the rotational velocity at the point of escape of the photon,  $\hat{k}$  is the photon's direction of propagation and  $v_{\text{th}}$  is the thermal velocity of the sphere. In this study we use  $v_{\text{th}} = 12.86$  km s $^{-1}$ , which corresponds to a temperature of  $T = 10^4$  K. We fix  $v_{\text{th}}$  throughout the paper, its influence is only of a multiplying constant that can be included without running new Monte-Carlo simulations, as the code works with the adimensional frequency  $x$ . However, the thermal velocity is considered a free parameter when comparing simulation results against observations.

The approach presented above allows us to produce new Ly $\alpha$  spectra and compare them with the full radiative transfer solution including both outflows and rotation.

## 3 RESULTS

### 3.1 Qualitative Trends

Figure 1 summarizes the most important trends from rhw RT simulations. In the left side, the six panels correspond to  $\tau = 10^6$  and a viewing angle of  $\theta = 90^\circ$ , that is, perpendicular to the rotation axis of the galaxy. In every panel the thin black line corresponds to the pure outflow solution, i.e. without rotation. From top to bottom we see the effect of increasing the outflow velocity, which is the expected increasing asymmetry towards the red peak.

The thick black line corresponds to the solution that includes both outflows and rotation. Comparing the left and right columns (lower versus higher rotational velocity) we can see two immediate effects. First, the line broadens and second, the intensity at the line's center increases.

The thick gray line corresponds to the pure outflow solution with the Doppler shift added to model rotation's influence. At  $\tau_{\text{H}} = 10^6$  the Doppler shift does a good job at capturing the broad morphological features introduced by rotation: the angle dependence, the broadening and the intensity increase at the line's center.

In the right side of Figure 1 we show the same results as in the left one, but for a viewing angle of  $\theta = 0^\circ$ , that is parallel to the rotation axis. In this case we confirm the result presented by [Garavito-Camargo et al. \(2014\)](#), namely that pure rotation introduces a strong dependence with viewing angle, a trend that we find also holds for rotation mixed with outflows.

The quality of the results from the Doppler shift improves for higher  $\tau_{\text{H}}$  values. In the Appendix we show the same plots as Figure 1, there it is evident that for  $\tau_{\text{H}} = 10^5$  the results are not as good as they are for  $\tau_{\text{H}} = 10^6$ , and

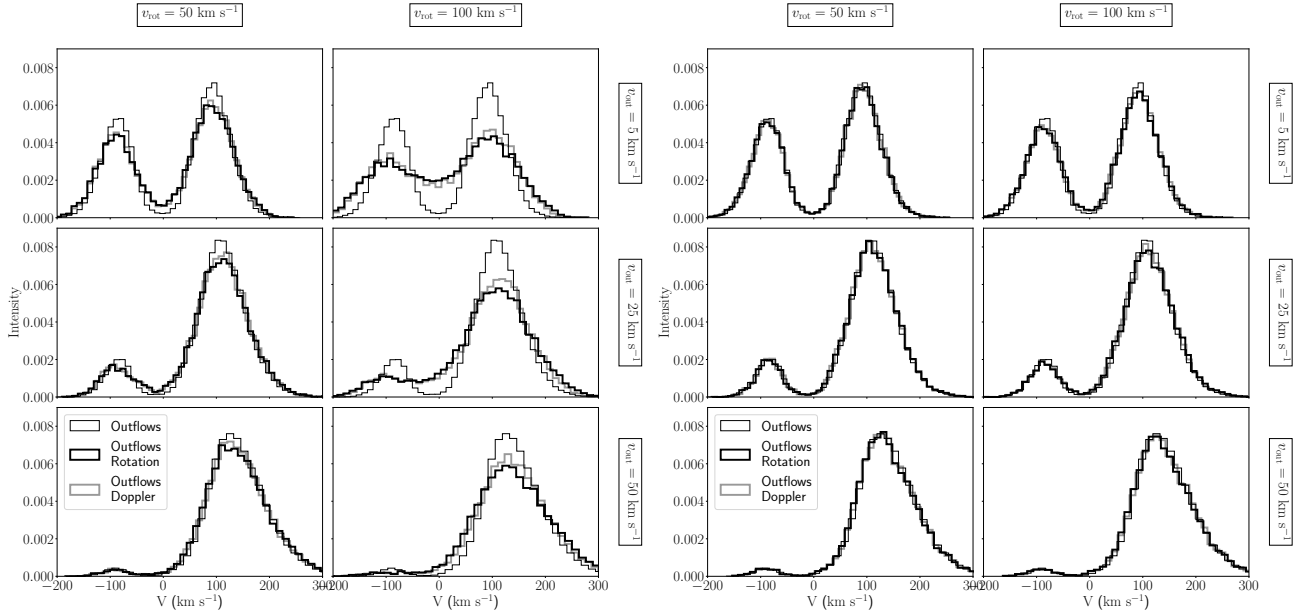


**Figure 1. Qualitative trends of changing outflow and rotational velocity viewed perpendicular/parallel to the rotation axis.** Here we fix  $\tau_H = 10^6$ . The six panels on the left correspond to  $\theta = 90^\circ$  and the panels on the right to  $\theta = 0^\circ$ . We vary  $v_{\text{rot}}$  increasing from left to right and  $v_{\text{out}}$  increasing from top to bottom. The thin black line corresponds to the Ly $\alpha$  line obtained with CLARA without any rotation and the indicated outflow velocity. The thick black line corresponds to the results including both outflows and rotation. The thick gray line shows the results of modifying the pure outflow solution by the Doppler shift presented in Equation 4 (in thin line), if there is a radiative transfer of rotation and outflows (thick and clear line), and if there is a radiative transfer of only outflows, but also a Doppler shift from the rotational velocity (thick and dark line).

that for  $\tau_H = 10^7$  the Doppler shift provides a remarkable good approximation.

### 3.2 Quantitative Trends

After finding the qualitative influence of the different parameters we move onto a quantitative study. To do this we summarize the line morphology by four different scalars: standard deviation (STD), skewness (SKW), bimodality (BI) and valley/peak ratio. These quantities are defined by the following equations (Kokoska & Zwillinger 1999):

$$\text{STD} = \sqrt{m_2}, \quad (5)$$

$$\text{SKW} = \frac{m_3}{m_2^{3/2}}, \quad (6)$$

$$\text{BI} = \text{KURTOSIS} - \text{SKW}^2 = \frac{m_4}{m_2^2} - \frac{m_3^2}{m_2^3}, \quad (7)$$

where each  $m_i$  is the  $i$ -th moment about the mean. The STD has velocity units and quantifies the line's width. The SKW is adimensional and quantifies the peaks' asymmetry. In the case of a bimodal distribution,  $\text{SKW} > 0$  means that the blue peak is taller and for  $\text{SKW} < 0$  the red peak is taller. The BI is adimensional and quantifies whether the line has 1 or 2 peaks: it is always  $\geq 1$  (Pearson 1929) and the closer to 1, the more bimodal is the line (i.e. has 2 similar peaks). We found by visual inspection of our spectra that  $\text{BI} = 2.5$  marks the transition between two peaks (however imbalanced) and a dominant single peak.

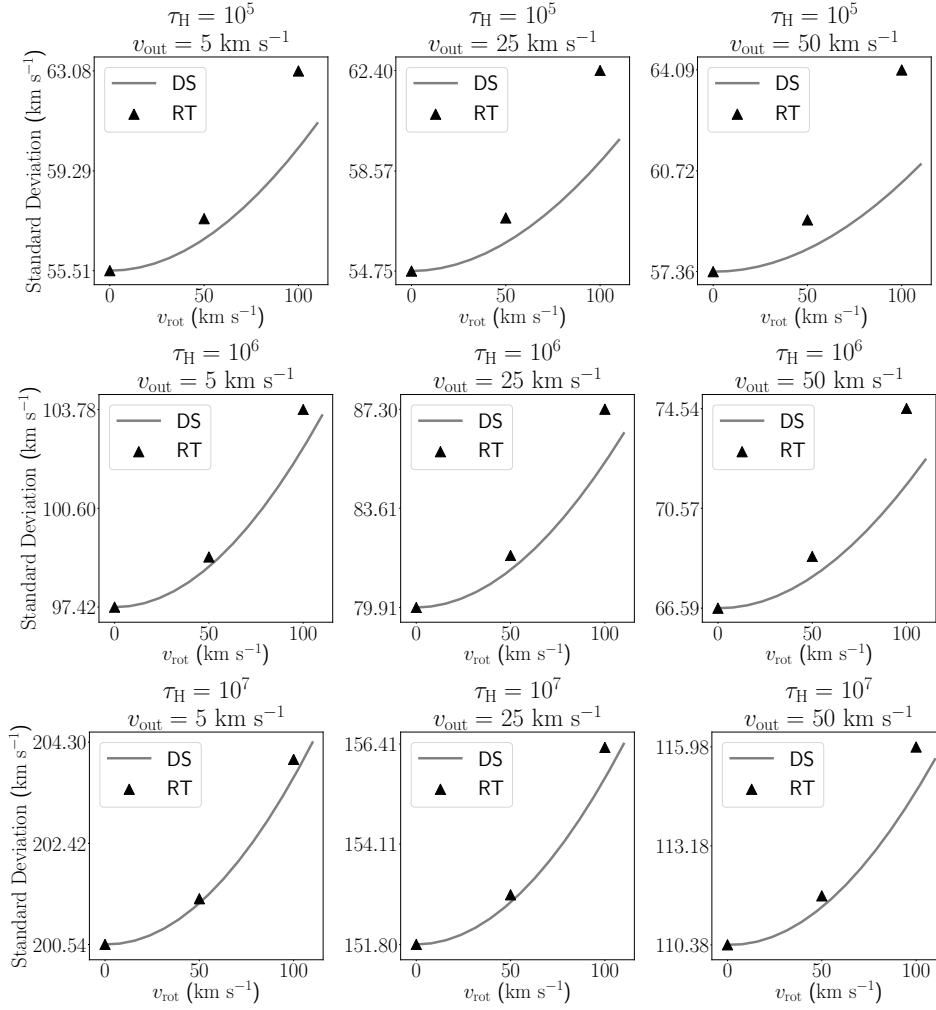
#### 3.2.1 Standard Deviation

Figure 2 summarizes the standard deviation results for all our models. Each panel shows the STD as a function of  $v_{\text{rot}}$ . All panels were computed using a viewing angle of  $\theta = 90^\circ$  (perpendicular to the rotation axis), which has the most extreme influence from rotation. The black triangles correspond to the full RT solution and the line to the DS approximation. The optical depth increases from top to bottom and the outflow velocity from left to right. This quantitative plot confirms that the line width increases with rotational velocity and optical depth. These trends are expected; higher rotational velocities can be seen as an addition of different Doppler shifts that smear out the line, while a higher optical depth translates into a larger number of scatterings that increase the probability of a photon to diffuse in frequency resulting in a broader line.

The DS successfully reproduces all trends with the optical depth, rotational velocity and outflow velocity. However, the DS consistently underestimates the STD. The difference between the RT and DS increases with the outflow velocity and the rotational velocity, and decreases with increasing optical depth. In the range of parameter space explored, this difference has as an upper bound of  $\sim 7\%$ ,  $3\%$  and  $\sim 2\%$  for  $\tau_H = 10^5$ ,  $10^6$  and  $10^7$ , respectively.

#### 3.2.2 Skewness

Figure 3 presents the skewness results for all the models together with the DS comparison following the same layout as Figure 2. In all cases the skewness is negative showing that all the lines are unbalanced towards the red side of



**Figure 2. Standard Deviation trends.** Results for all the Radiative Transfer simulations (in triangles) compares against the Doppler Shift model (lines). All panels correspond to a viewing angle of  $\theta = 90^\circ$  (perpendicular to the rotation axis). The optical depth increases from top to bottom and the outflow velocity from left to right.

the spectrum. Skewness increases with rotational velocity and decreases with optical depth; rotation tries to smooth the line diminishing the asymmetries while a higher optical depth reinforces the line asymmetries. The skewness does not have a monotonous trend with outflow velocity because there is a transition between double and single peak line; for low outflow velocities the skewness signals the balance between the two existing peaks while for high outflow velocities it quantifies the asymmetry of the already dominant read peak.

The DS reproduces the main trends, again with an underestimation that decreases at higher optical depths and increases with larger values of the rotational velocity and outflow velocity. In this case the differences between RT and DS have an upper bound of 85%, 35% and 5% for  $\tau_H = 10^5$ ,  $10^6$  and  $10^7$ , respectively.

### 3.2.3 Bimodality

Figure 4 shows the results for the bimodality using the same layout as in the two previous Figures. Following the

reasoning about the skewness, we observe that increasing the outflow velocity increases the value of bimodality, that is, it transitions to a more pronounced single peak. The trend as a function of the rotational velocity and the optical depth are not monotonous. When the outflow velocity is low ( $v_{\text{out}} < 50 \text{ km s}^{-1}$ ), an increasing rotational velocity smears the two asymmetrical peaks pushing the line morphology towards a single peaks, making the bimodality statistics increase. On other situations ( $v_{\text{out}} = 50 \text{ km s}^{-1}$  and  $\tau_H \geq 10^6$ ) higher rotational velocities the bimodality statistics decreases, which means that it manages to slightly enlarge the already dominant red peak.

The DS reproduces the main trends while underestimating the bimodality statistics. As expected from the previous results the difference between RT and DS decreases at higher optical depths and increases with increasing values of the rotational and outflow velocities. In this case the differences have an upper bound of 4%, 2% and 1% for  $\tau_H = 10^5$ ,  $10^6$  and  $10^7$ , respectively.

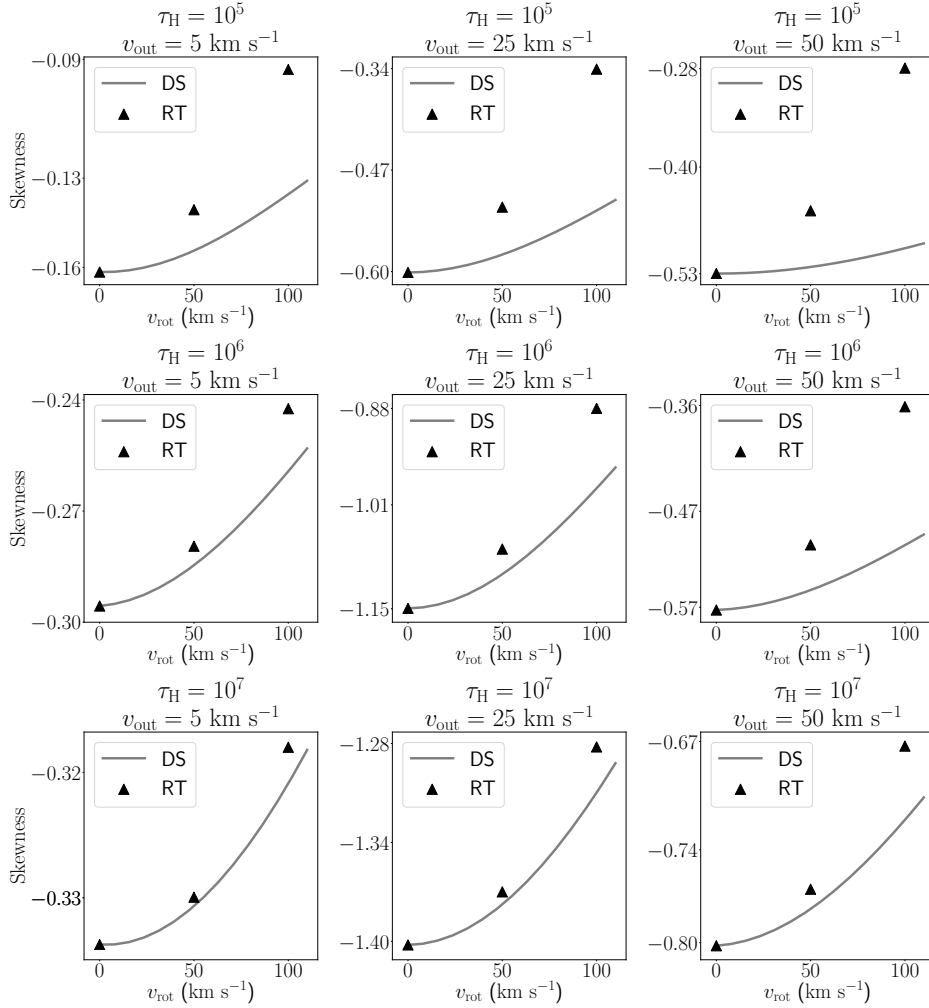


**Figure 3. Skewness trends.** Results for all the Radiative Transfer simulations (in triangles) compares against the Doppler Shift model (lines). Follows the same layout as Figure 2.

### 3.2.4 Intensity at line's center

In Figure 5 we quantify how the intensity at the line's center (i.e. the valley) changes with the viewing angle, the outflow velocity and the optical depth. These results correspond to a fixed rotational velocity of  $v_{\text{rot}} = 100 \text{ km s}^{-1}$ . The triangles correspond to the RT simulations and the line represents the DS results. The valley intensity is expressed as a fraction of the maximum peak intensity in the line, as such the valley/peak ratio is always  $< 1$ . In every panel we see that the valley/peak ratio decreases as the observer moves from a line of sight perpendicular to the rotation axis onto a parallel line of sight. This is a clear demonstration of the viewing angle dependency introduced by rotation.

The valley/peak ratio at  $\cos\theta = 1$  matches results without rotation, this shows that for increasing rotational velocity the valley/peak ratio increases. In turn, for increasing optical depth or outflowing velocity this ratio decreases. Once again, the DS results correctly follow the trends for the full RT simulations. This time the differences have an upper bound of 55%, 2% and 1% for  $\tau_H = 10^5$ ,  $10^6$  and  $10^7$ , respectively.

## 4 DISCUSSION

In this section we discuss how the results we have presented can be connected to the interpretation of observational data.

### 4.1 Ly $\alpha$ continuum leakage or rotation?

One application of this new model to the current interpretation of Ly $\alpha$  spectra, is that the central ( $V = 0$ ) emission of the spectra seen in the Ly $\alpha$  line, is a consequence of the viewing angle of the galaxy and can be controlled by it. Several authors have suggested that this central emission is caused by radiation that escapes the galaxy without scattering, mostly due to a clumpy interstellar medium (Hansen & Oh 2006; Gronke et al. 2016). Rotation is an alternative that solves this issue.

We note that the relative intensity of the two peaks in the outflowing spectra is not modified by rotation, that asymmetry is solely controlled by the outflow velocity. This means that results that have already derive a typical outflowing velocity as to match the observational constraints do not have to be completely revised. Only an additional

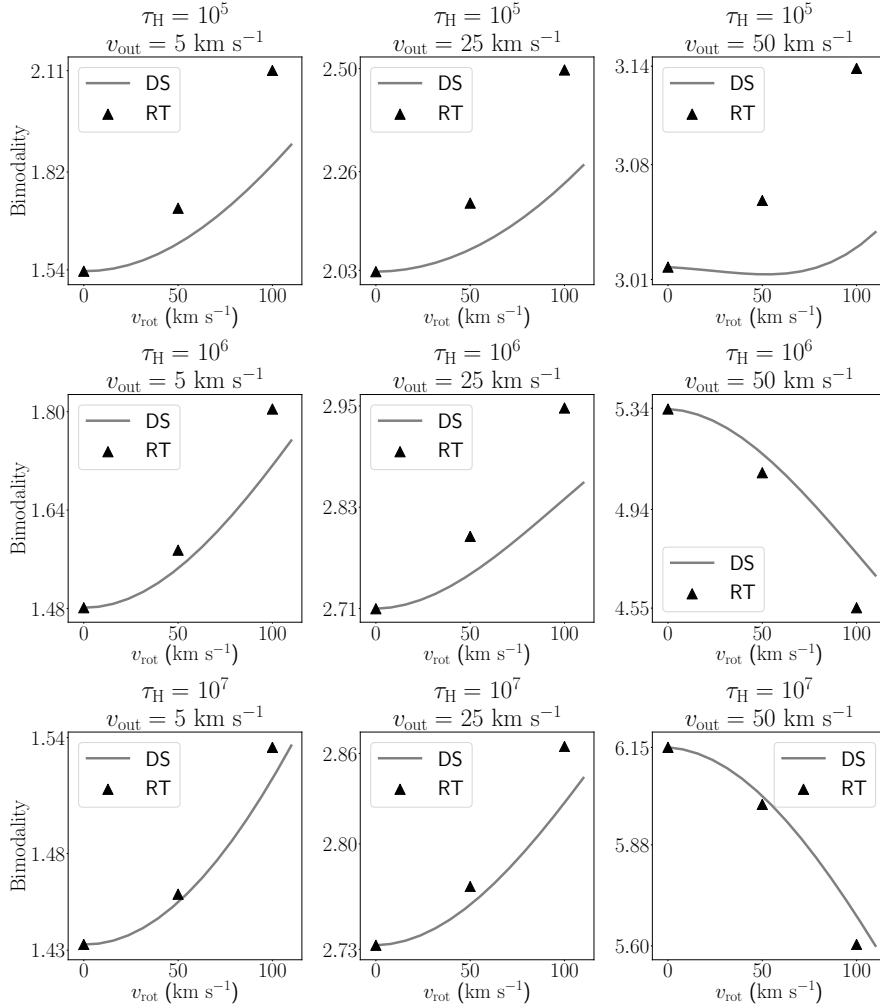


**Figure 4. Bimodality trends.** Results for all the Radiative Transfer simulations (in triangles) compares against the Doppler Shift model (lines). Follows the same layout as Figure 2.

exploration of rotational velocities and viewing angles needs to be explored.

A recent observational example is provided by [Rivera-Thorsen et al. \(2017\)](#). They report optical spectroscopy of a bright lensed galaxy at a redshift of  $z = 2.4$ . The object presents a triple peaked  $\text{Ly}\alpha$  profile that can be thought as the superposition of two components, a double asymmetric peak and a narrower symmetric peak around the line's center. One possible option for the narrow component is that it escaped the galaxy without substantial interaction with neutral Hydrogen. We speculate that the central feature could also be due to a purely rotating component that can produce such a feature as shown by [Forero-Romero et al. \(2018\)](#). The triple peak could be then produced by two main decoupled components: one rotating the other outflowing.

Another interesting example are the  $\text{Ly}\alpha$  lines in Green Pea galaxies ([Yang et al. 2016](#)). [Yang et al. \(2017\)](#) showed in a study of 43 Green Pea galaxies that 2/3 were strong  $\text{Ly}\alpha$  emitters. There the  $\text{Ly}\alpha$  escape fraction is effectively estimated from the ratio of  $\text{H}\alpha$  to  $\text{Ly}\alpha$ . Galaxies with large escape fractions also substantial  $\text{Ly}\alpha$  emission at the line's center. We speculate that this feature could help to constrain

rotation in Green Pea galaxies and find new correlations between  $\text{Ly}\alpha$  escape fraction and galaxy rotation.

## 4.2 $\text{Ly}\alpha$ Kinematic Maps

Current observational facilities have the capability of spatially resolving the extent of a LAE. For instance [Prescott et al. \(2015\)](#) presented observational results of a Doppler shift when taking spectra at two opposite sides of a large ( $\approx 80\text{kpc}$ ) LAE. In more recent work [Arrigoni Battaia et al. \(2018\)](#) mapped  $\text{Ly}\alpha$  emission around a quasar.

In Figure 6 we present a toy model ( $v_{\text{rot}} = 50 \text{ km s}^{-1}$ ,  $v_{\text{out}} = 25 \text{ km s}^{-1}$  and  $\tau_{\text{H}} = 10^5$ ) for the spectrum of a LAE taken from two different sides of the galaxy. As the LAE is rotating, one side is being redshifted while the other is blueshifted. We see that the full spectrum is a weighted line, in solid black, that is found between these two. We notice that the distance between the maxima of the blue and red spectra is not twice the rotational velocity as it could be naively expected.

Although it is a good approximation to think the rotating spectra by a sum of Doppler shifts, the peak of the



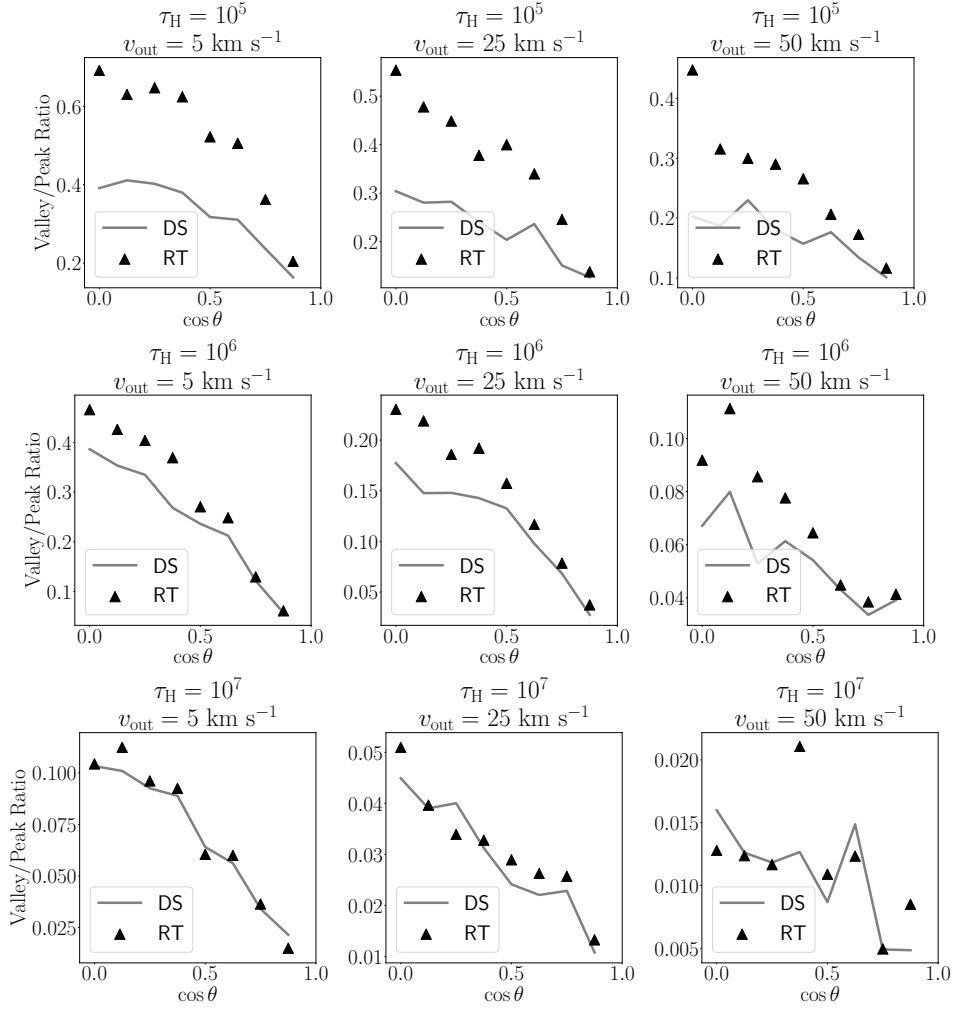


**Figure 5. Valley Intensity.** We show for each  $\tau_H$  the dependency that the viewing angle  $\theta$  has on the line's the valley intensity.  $v_{\text{rot}} = 100 \text{ km s}^{-1}$  is fixed for all panels.

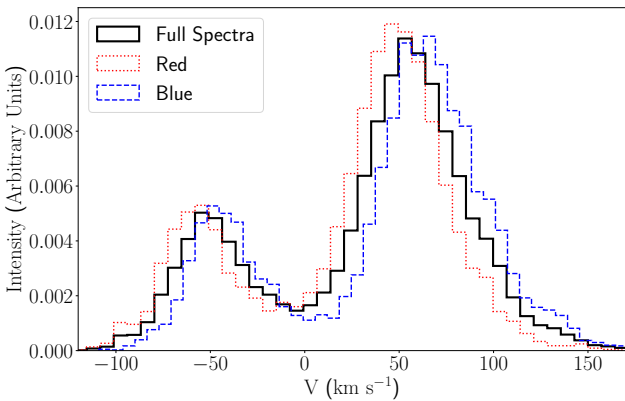


**Figure 6. Spectra from receding/approaching sides of a toy model LAE.** These results correspond to the RT simulation with  $v_{\text{out}} = 25 \text{ km s}^{-1}$ ,  $v_{\text{rot}} = 50 \text{ km s}^{-1}$ ,  $\tau_H = 10^5$ . The spectra were computed for a viewing angle of  $\theta = 90^\circ$ . This toy model illustrates to what extent spectra from opposite sides of a galaxy have an imprint of the rotational kinematics.

spectra is also weighted by the amount of mass with a given line-of-sight velocity. In this toy model the distance between the peaks of the receding/approaching spectra is close to  $\sim 20 \text{ km s}^{-1}$ , which is less than half of the naively expected value of  $2v_{\text{rot}} = 100 \text{ km s}^{-1}$ , due to the fact that only a small fraction of the photons are emitted at the extreme of the galaxy having the maximum rotational velocity of  $50 \text{ km s}^{-1}$ .

Spectrographs like the Multi Unit Spectroscopic Explorer (MUSE) could obtain kinematic information from large samples of LAEs to build velocity maps in Ly $\alpha$ . This could be a natural extension of the work reported by [Hernandez et al. \(2016\)](#) on the velocity maps of several LARS (Lyman Alpha Reference Sample) galaxies. The interpretation of such data should take into account the insights and trends we have presented in this paper.

### 4.3 Comparison against the MUSE-Wide Survey

In order to give the reader a feeling of the ranges of observational data that could be explained by the models presented

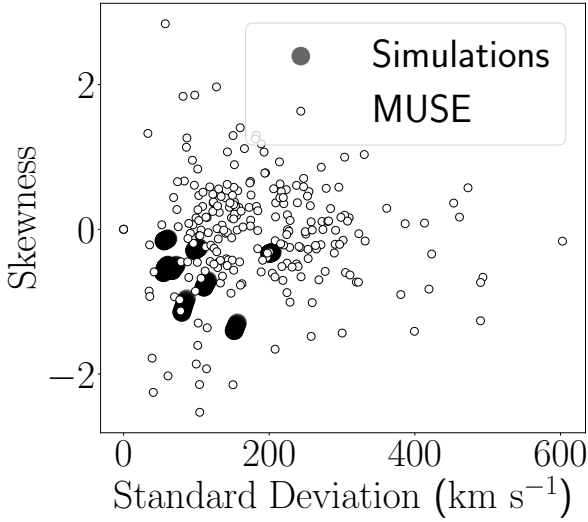


**Figure 7. Comparison between simulations and observations.** The observational results correspond to the MUSE-Wide Survey (Herenz et al. 2017). The skewness and standard deviation from the simulations summarize the results presented in Figures 2 and 3.

here, we perform a comparison against observational data from the MUSE-Wide Survey (MWS) (Herenz et al. 2017).

MWS provides public access to 831 spectra out of which 237 contain a detected Ly $\alpha$  line as dominant. The public dataset reports as the redshift of the galaxy the position of the dominant peak. We use this redshift to convert the spectra to a rest-frame and compute the standard deviation and skewness statistics. Given the uncertainty on the galaxy redshift we do not compute the valley/peak ratio. We do not try to perform a full fit to all the spectra (e.g. Gronke 2017) and wish only to know whether the region of parameter space explored in our RT simulations shows any crossing with the results from the MWS or shows any sign of atypical features.

Figure 7 shows the results of this experiment. The small white circles correspond to the 217 Ly $\alpha$  emitters in the MWS observations; the large black circles to the results of the simulations presented in this paper. This shows that the systems modeled in this paper actually present an overlap with statistics derived from observations. The region with standard deviation  $> 200 \text{ km s}^{-1}$  could also be explained by systems with larger optical depths than we have used here. However, the systems with a positive skewness, that is a line unbalanced towards the blue could be the sign of inflowing kinematics.

#### 4.4 Low optical thickness regimes

When located in the regimes of low optical thickness,  $\tau_H \lesssim 4$ , the agreement of the radiative transfer simulation with the semi-analytical solution is not as accurate. In this regime, only numerical simulations can help to predict the shape of the Ly $\alpha$  profiles. We ran a simulation with low  $\tau_H$  and compared it with the semi-analytical model. As seen in Figure 8, the model does not fit the simulation. This creates physical restrictions on the input of our model.

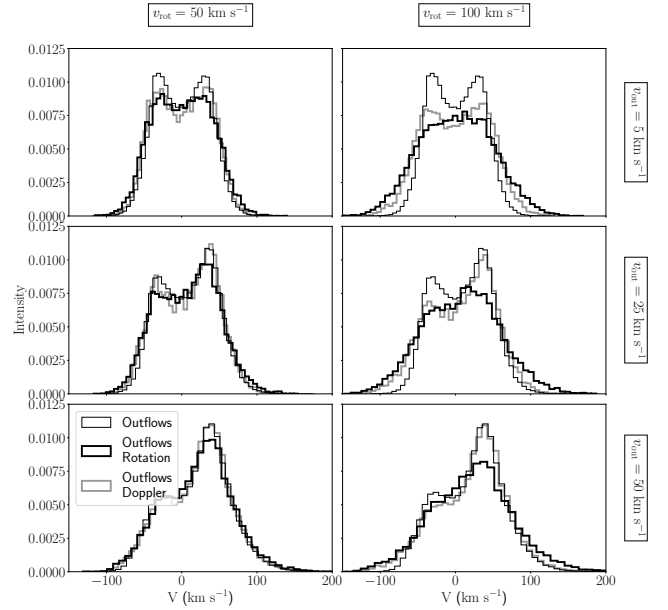


**Figure 8. Low optical thickness regimes.** Here we fix  $\tau_H = 10^4$ . The six panels correspond to  $\theta = 90^\circ$ . We vary  $v_{\text{rot}}$  increasing from left to right and  $v_{\text{out}}$  increasing from top to bottom. The thin black line corresponds to the Ly $\alpha$  line obtained with CLARA without any rotation and the indicated outflow velocity. The thick black line corresponds to the results including both outflows and rotation. The thick gray line shows the results of modifying the pure outflow solution by the Doppler shift presented in Equation 4 (in thin line), if there is a radiative transfer of rotation and outflows (thick and clear line), and if there is a radiative transfer of only outflows, but also a Doppler shift from the rotational velocity (thick and dark line).

## 5 CONCLUSIONS

In this paper we explore, for the first time in the literature, the results of a model for the emergent Ly $\alpha$  line from rotating outflows. The main results for the model are computed from a Monte-Carlo radiative transfer simulation and confronted with a simple semi-analytic ansatz that adds the effects of rotation onto results of pure outflow kinematics.

To address the first question we posed in the introduction (*what is then the expected imprint of rotation on a resonant emission line such as the Ly $\alpha$  line?*) we can say that the main effects of rotation on the Ly $\alpha$  line morphology are:

- Inducing a dependency on the viewing angle.
- Broadening the line.
- Increasing the intensity at the line's center.

We find that these effects can be quantitatively explained by a Doppler shift computed as product of quantities at the surface of last scattering, namely  $\vec{v}_{\text{rot}} \cdot \hat{k}$ , where  $\vec{v}_{\text{rot}}$  is the velocity due to rotation and  $\hat{k}$  is the direction of the photon's propagation. These conclusions, specially the confirmation of the Doppler shift as a good approximation to model solid body rotation, strengthen the semi-analytic model reported by Garavito-Camargo et al. (2014) where they modeled the effect of pure rotation on Ly $\alpha$  spectra.

Addressing the second question we posed in the introduction (*to what extent is it possible to constrain rotational kinematics from the Ly $\alpha$  emission line?*) we can say that



as an application to observational data our results suggest that rotation should also be considered as an explanation of the non-vanishing Ly $\alpha$  intensity at the line's center, which could change the interpretation of recent observational results (e.g. [Yang et al. 2017](#); [Rivera-Thorsen et al. 2017](#)) and provide a test for rotation in the observed systems.

A more straightforward approach takes into account how the Ly $\alpha$  spectra from two different sides of a galaxy can detect approaching/receding gas motions ([Prescott et al. 2015](#); [Arrigoni Battaia et al. 2018](#)). In that case, one has to be careful and take into account that the peaks of these two spectra is smaller than the expected value of  $2 \times v_{\text{rot}}$  due to the different weights at the surface of the emitting regions.

We also use data from MUSE ([Herenz et al. 2017](#)) to show to what extent the outputs of the RT results presented here can be expected to match hundreds of observed Ly $\alpha$  spectra, but a full constraint of rotational properties certainly requires a full Markov Chain Monte Carlo exploration of parameter space.

Our work confirms that rotation produces features in the Ly $\alpha$  line strong enough that can be expected to be detected in observations and that should be taken into account into Ly $\alpha$  modeling; the Doppler Shift offers an easy-to-implement approximation to explore such influence into already existing RT simulations and provide stronger footing to the interpretation of present and future Ly $\alpha$  kinematics maps (e.g. [Arrigoni Battaia et al. 2018](#)).

## References

- Ahn S.-H., Lee H.-W., Lee H. M., 2003, [MNRAS](#), **340**, 863
- Arrigoni Battaia F., Prochaska J. X., Hennawi J. F., Obreja A., Buck T., Cantalupo S., Dutton A. A., Macciò A. V., 2018, [MNRAS](#), **473**, 3907
- Cairós L. M., González-Pérez J. N., 2017, [A&A](#), **600**, A125
- Cairós L. M., Caon N., Weilbacher P. M., 2015, [A&A](#), **577**, A21
- Dijkstra M., Haiman Z., Spaans M., 2006, [ApJ](#), **649**, 14
- Erb D. K., et al., 2014, [ApJ](#), **795**, 33
- Forero-Romero J. E., Yepes G., Gottlöber S., Knollmann S. R., Cuesta A. J., Prada F., 2011, [MNRAS](#), **415**, 3666
- Forero-Romero J. E., Gronke M., Remolina-Gutiérrez M. C., Garavito-Camargo N., Dijkstra M., 2018, [MNRAS](#), **474**, 12
- Garavito-Camargo J. N., Forero-Romero J. E., Dijkstra M., 2014, [ApJ](#), **795**, 120
- Gronke M., 2017, [A&A](#), **608**, A139
- Gronke M., Bull P., Dijkstra M., 2015, [ApJ](#), **812**, 123
- Gronke M., Dijkstra M., McCourt M., Oh S. P., 2016, [ApJ](#), **833**, L26
- Hansen M., Oh S. P., 2006, [MNRAS](#), **367**, 979
- Herenz E. C., et al., 2016, [A&A](#), **587**, A78
- Herenz E. C., et al., 2017, [A&A](#), **606**, A12
- Kokoska S., Zwillinger D., 1999, CRC standard probability and statistics tables and formulae. Crc Press
- Orsi A., Lacey C. G., Baugh C. M., 2012, [MNRAS](#), **425**, 87
- Partridge R. B., Peebles P. J. E., 1967, [ApJ](#), **147**, 868
- Pearson K., 1929, *Biometrika*, **21**, 370
- Prescott M. K. M., Martin C. L., Dey A., 2015, [ApJ](#), **799**, 62
- Rivera-Thorsen T. E., et al., 2017, [A&A](#), **608**, L4
- Steidel C. C., Erb D. K., Shapley A. E., Pettini M., Reddy N., Bogosavljević M., Rudie G. C., Rakic O., 2010, [ApJ](#), **717**, 289
- Trainor R. F., Strom A. L., Steidel C. C., Rudie G. C., 2016, [ApJ](#), **832**, 171
- Verhamme A., Schaerer D., Maselli A., 2006a, [A&A](#), **460**, 397
- Verhamme A., Schaerer D., Maselli A., 2006b, [A&A](#), **460**, 397

- Yamada T., Matsuda Y., Kousai K., Hayashino T., Morimoto N., Umemura M., 2012, [ApJ](#), **751**, 29
- Yang H., Malhotra S., Gronke M., Rhoads J. E., Dijkstra M., Jaskot A., Zheng Z., Wang J., 2016, [ApJ](#), **820**, 130
- Yang H., et al., 2017, [ApJ](#), **844**, 171

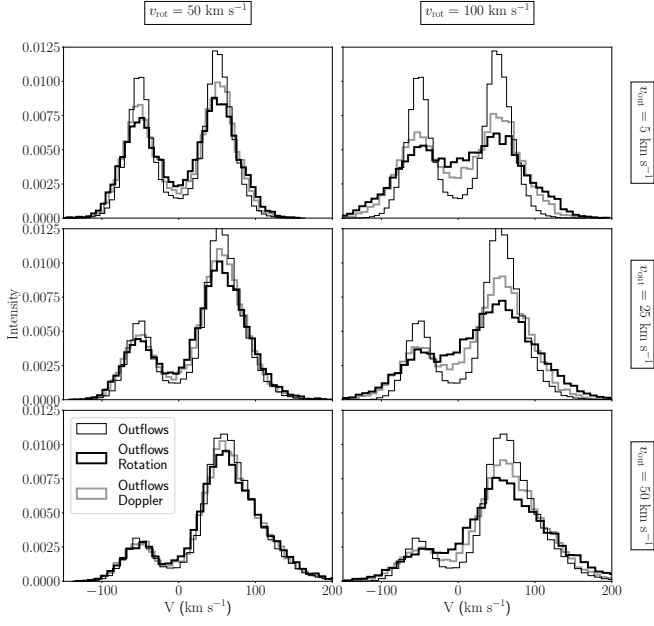


**Figure A1.** Qualitative trends of changing outflow and rotational velocity. Same layout as Figure 1, this time  $\tau_H = 10^5$  and  $\theta = 90^\circ$ .

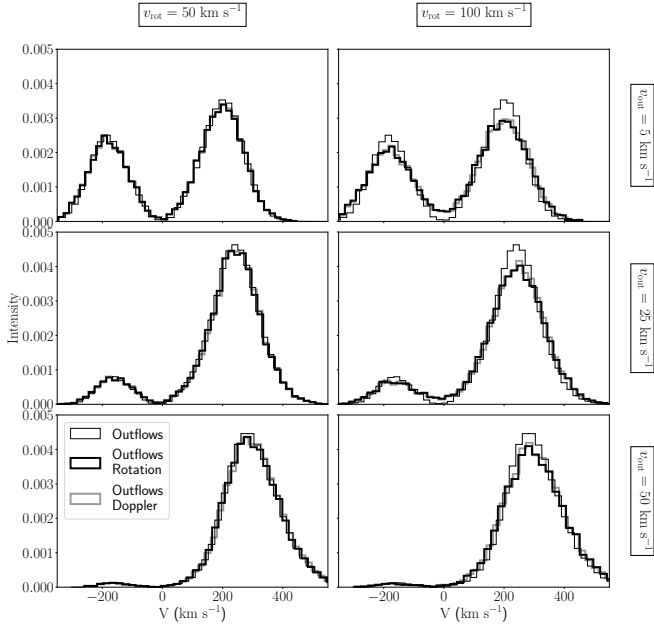


**Figure A2.** Qualitative trends of changing outflow and rotational velocity. Same layout as Figure 1, this time  $\tau_H = 10^7$  and  $\theta = 90^\circ$ .

## APPENDIX A: ADDITIONAL FIGURES